



# IrNi nanoparticle-decorated flower-shaped NiCo<sub>2</sub>O<sub>4</sub> nanostructures: controllable synthesis and enhanced electrochemical activity for oxygen evolution reaction

Zhifan Chen<sup>1</sup>, Hongbin Zhao<sup>1\*</sup>, JiuJun Zhang<sup>1</sup> and Jiaqiang Xu<sup>1,2\*</sup>

**ABSTRACT** In this work, we demonstrated the enhanced oxygen evolution reaction (OER) activity of flower-shaped cobalt-nickel oxide (NiCo<sub>2</sub>O<sub>4</sub>) decorated with iridium-nickel bimetal as an electrode material. The samples were prepared by carefully depositing pre-synthesized IrNi nanoparticles on the surfaces of the NiCo<sub>2</sub>O<sub>4</sub> nano-flowers. Compared with bare NiCo<sub>2</sub>O<sub>4</sub>, IrNi, and IrNi/Co<sub>3</sub>O<sub>4</sub>, the IrNi/NiCo<sub>2</sub>O<sub>4</sub> exhibited significantly enhanced electrocatalytic activity in the OER, including a lower overpotential of 210 mV and a higher current density at an overpotential of 540 mV. We found that the IrNi/NiCo<sub>2</sub>O<sub>4</sub> showed more efficient electron transport behavior and reduced polarization because of its bimetal IrNi modification by analyzing its Tafel slope and turnover frequency. Furthermore, the electrocatalytic mechanism of IrNi/NiCo<sub>2</sub>O<sub>4</sub> in the OER was studied, and it was found that the combined active sites of the composite effectively improved the rate determining step. The synergic effect of the bimetal and metal oxide plays an important role in this reaction, enhancing the transmission efficiency of electrons and providing more active sites for the OER. The results reveal that IrNi/NiCo<sub>2</sub>O<sub>4</sub> is an excellent electrocatalyst for OER.

**Keywords:** electrocatalysis, OER, bimetal

## INTRODUCTION

Traditional fossil fuels are in increasingly short supply and their use presents serious environmental problems. Therefore, new renewable sources of energy like oxygen and hydrogen have attracted increasing research attention [1–3]. The oxygen evolution reaction (OER) is a half-reaction of water splitting and is one of the most common methods to procure oxygen, which is widely used as the cathode energy

source in fuel cells [4–9]. Therefore, it is extremely important for researchers to develop catalysts with enhanced current and decreased overpotential in order to meet increasing demands for energy.

Noble metals and metallic oxides have been thoroughly studied owing to their relatively low overpotentials. Iridium [10] and iridium-based materials have been applied as catalysts in the OER [6,11]; however, their high cost hinders their application and development. Recently, non-noble metal and metallic oxide catalysts, especially those based on transition elements such as cobalt [1,12–16] and nickel [17–19], have been shown to exhibit interesting catalytic activity in the OER. Their long-term resistance to corrosion in alkaline solution [20] and unique properties are important factors. Liang *et al.* [15] reported Co<sub>3</sub>O<sub>4</sub> nanocrystals on graphene as a synergistic catalyst for OER with high activity. Friebe *et al.* [19] also reported that (Ni, Fe)OOH as an electrocatalyst for water splitting exhibited good activity in the OER. Furthermore, according to the published mechanism [21], hydrous anodic oxides with amphoteric character like cobalt-based and nickel-based catalysts possess higher activity.

In the field of electrochemistry, no single element or compound has yet provided the required performance. However, hybrid and composite materials have been synthesized that combine the unique characters of each component to surpass the limitations of the single materials, and preferable performance has been achieved [22–25]. Synergic effects or weak interactions usually perform major roles [26,27]. Transition metals and noble metals each have their own advantages and drawbacks. To develop

<sup>1</sup> Department of Chemistry, Shanghai University, Shanghai 200444, China

<sup>2</sup> State Key Laboratory of Transducer Technology, Shanghai Institute of Microsystem and Information Technology, Chinese Academy of Sciences, Shanghai 200050, China

\* Corresponding authors (emails: hongbinzhao@shu.edu.cn (Zhao H); xujiaqiang@shu.edu.cn (Xu J))

more efficient materials for use in water splitting we can use the method of compounding. Bimetallic materials are a special kind of composites and can form alloy structures with enhanced activities [28,29]. Through a combination of multiple approaches, it is possible to improve the activity of catalysts for the OER.

In the present work, we designed a three-dimensional (3D) flower-shaped  $\text{NiCo}_2\text{O}_4$  nanostructure decorated with IrNi alloy nanoparticles. Here, we use the noble metal Ir and the transition metal Ni to synthesize the bimetallic alloy to lessen the need for noble metals, because vacant orbitals and d electrons are plentiful in Ir. While Ni is one of the first-row transition metals (including Fe, Co, and Ni), it has excellent activity towards the OER, as mentioned above, so it can also act as an active site in the reaction and interact with  $\text{NiCo}_2\text{O}_4$  weakly through metal–oxygen (M–O) interactions. The electrocatalytic activity of the synthesized IrNi/ $\text{NiCo}_2\text{O}_4$  is greatly enhanced, and the overpotential is effectively lowered by the introduction of IrNi alloy nanocrystals to the catalyst. The electrochemical mechanism was studied by detailed experimental analysis.

## EXPERIMENTAL SECTION

### Synthesis of IrNi alloy nanoparticles

In a typical procedure, iridium trichloride hydrate and nickel chloride hexahydrate at a stoichiometric ratio of 1:1 were added to a 50-mL round-bottom flask containing 20 mL of oleylamine at 120°C in an oil bath. The homogeneous solution was treated for 10 min each at 160, 180, 200, and 240°C with stepwise temperature increase under continuous stirring. After the reactor was cooled to room temperature, the product was centrifuged, washed with a mixture of *n*-hexane and absolute ethanol several times, and dried at 60°C overnight.

### Synthesis of flower-shaped $\text{NiCo}_2\text{O}_4$

Typically, 1.5 mmol cobalt chloride hexahydrate, 0.75 mmol nickel chloride hexahydrate, and 45 mmol urea were dissolved in 50 mL water. Then, the mixed solution was stirred for 20 min at room temperature to form a homogeneous solution. The solution was then transferred into a 250-mL three-necked flask and 70 mL ethylene glycol was added. The solution was treated with microwave irradiation in a 320-W XH-MC-1 microwave reactor at 110°C for 15 min. The precipitate was obtained by centrifuging and washed thoroughly with distilled water and absolute ethanol several times once the reaction had cooled to room temperature. Finally, black  $\text{NiCo}_2\text{O}_4$  powders were obtained by heat-treating the product collected above at

60°C overnight and 300°C for 2 h in a muffle furnace.

### Preparation of IrNi/ $\text{NiCo}_2\text{O}_4$ composite

First, we coated IrNi bimetal nanoparticles onto a reagent glass with ethanol, and dispersed them uniformly under ultrasonic irradiation for 2 h. Then,  $\text{NiCo}_2\text{O}_4$  was added to the obtained suspension at a weight ratio of 4:1 ( $\text{NiCo}_2\text{O}_4$ :IrNi = 4:1). After dispersing the  $\text{NiCo}_2\text{O}_4$  nanoparticles with ultrasound for further 2 h, the IrNi/ $\text{NiCo}_2\text{O}_4$  composite was obtained by drying at 70°C until the ethanol was volatilized completely.

### Materials characterization

The crystalline structure of the  $\text{NiCo}_2\text{O}_4$  sample was determined by powder X-ray diffraction (XRD) measurements with a Rigaku D-MAX/IIA X-ray diffractometer within a scanning range of 5–70° ( $2\theta$ ) at a rate of 1.2° ( $2\theta$ )  $\text{min}^{-1}$  under Cu  $K\alpha$  radiation. The microstructure of IrNi,  $\text{NiCo}_2\text{O}_4$ , and IrNi/ $\text{NiCo}_2\text{O}_4$  was observed with scanning electron microscopy (SEM) (JMS-6700F), transmission electron microscopy (TEM) (JEM-2010F) and high-resolution TEM (HRTEM) (FEI-TECNAIG2F20), (JEM-2100F). Subsequently, the elemental composition and bonding configurations of the catalysts were measured by X-ray photoelectron spectroscopy (XPS) (ESCALAB 250Xi).

### Electrochemical measurements

A standard three-electrode system comprising a glassy carbon electrode (GCE) as a working electrode, a saturated calomel electrode (SCE) as a reference electrode, and a platinum wire as a counter electrode was connected to an electrochemical workstation (CorrTest CS330), which was utilized to study the electrochemical performance of the catalysts. Linear sweep voltammetry (LSV) measurements with a scan rate of 5  $\text{mV s}^{-1}$  at room temperature were adopted to evaluate the electrochemical performances of the catalysts, including overpotential and current density. The working electrode was fabricated as follows: 4 mg of catalyst was dispersed by sonication into a mixture of 180  $\mu\text{L}$  of ethanol and 180  $\mu\text{L}$  of deionized water. After sonication for 30 min, 40  $\mu\text{L}$  of 0.5 wt.% Nafion in ethanol was added to the above ink, and it was sonicated for another 15 min. Then, 5  $\mu\text{L}$  of catalyst ink was dropped onto the surface of GCE as the working electrode. A solution of 0.1  $\text{mol L}^{-1}$  KOH was used as the electrolyte, and bubbled with high-purity nitrogen ( $\text{N}_2$ ) for 30 min prior to use.

All the potential data were converted to those of a reversible hydrogen electrode (RHE) using the formula  $E_{\text{RHE}} = E_{\text{SCE}} + 0.242\text{V} + 0.059\text{pH}$ . The overpotential  $\eta$  equals the RHE potential minus the standard electrode potential of

oxygen ( $\eta = E_{\text{RHE}} - 1.23\text{V}$ ). For further comparison and study, the amount of catalyst loaded in this work was calculated as  $0.212 \text{ mg cm}^{-2}$ .

## RESULTS AND DISCUSSIONS

As shown in Fig. 1a, all the peaks of the synthesized sample correspond to spinel  $\text{NiCo}_2\text{O}_4$  phase (JCPDS card no.20-0781) including the (111) plane, (200) plane, and (311) plane. Thus, it is clear that spinel  $\text{NiCo}_2\text{O}_4$  can be successfully prepared by a microwave-assisted reaction. The XRD pattern of IrNi in Fig. 1a also shows that IrNi alloy has been synthesized because the diffraction peaks are between those of the two metal components (Ir and Ni), indicating a new crystal formation. These XRD patterns indicate the successful synthesis of  $\text{NiCo}_2\text{O}_4$  and IrNi alloy. Further elemental analysis will be presented below. The SEM image in Fig. 1b shows that  $\text{NiCo}_2\text{O}_4$  presents a flower-shaped 3D structure assembled by a number of flexible nanoflakes. The size of the flower-shaped  $\text{NiCo}_2\text{O}_4$  nanostructures is  $\sim 20 \mu\text{m}$ . More SEM images are available in Fig. S2. Clearly, urea, ethylene glycol, and the microwave-assisted preparation play indispensable roles in the morphology of the products [30,31].

After decorating, scanning TEM (STEM) and HRTEM were employed to observe the fine microstructure and composition of the synthesized sample. As shown in Fig. 2, the IrNi/ $\text{NiCo}_2\text{O}_4$  composite contains Ni (Fig. 2e), Co (Fig. 2d), O (Fig. 2b), and relatively low contents of Ir (Fig. 2c). In Fig. 2f, the appearance of “flake-like” morphology illustrates the existence of ultra-thin flakes of  $\text{NiCo}_2\text{O}_4$ . This flake-shaped structure not only provides support for the uniform distribution of bimetal IrNi, but also offers more active sites for  $-\text{OH}$  adsorbance owing to the thin “petals”. In Fig. 3a, the larger magnification image of IrNi/ $\text{NiCo}_2\text{O}_4$  provides data for the lattice fringe. The lattice spacing of

$2.43 \text{ \AA}$ ,  $2.83 \text{ \AA}$  and  $4.37 \text{ \AA}$  correspond to the lower index (111), (220), (311) crystal planes of  $\text{NiCo}_2\text{O}_4$ , respectively [32]. Interestingly, another two types of lattice fringes are found in the HRTEM images, and we have assigned them to IrNi nanoparticles. Therefore, we can safely confirm that bimetallic IrNi has been loaded onto the  $\text{NiCo}_2\text{O}_4$  nanoflakes. Fig. 3b is an HRTEM image of the as-synthesized monodispersed pure IrNi nanoparticles with a grain size of approximately 10 nm. We also performed selected area electron diffraction (SAED) for IrNi/ $\text{NiCo}_2\text{O}_4$ , as shown in Fig. S3, and the composite exhibits polycrystalline morphology. The 3D-flower microstructure of IrNi/ $\text{NiCo}_2\text{O}_4$  may provide enhanced activity towards the OER.

Furthermore, XPS spectroscopy is a method for exploring the components and valence of each element, and we utilized it to predict the potential active sites and reveal their catalytic mechanism. The full survey spectrum (Fig. 4a) verifies the presence of Ni, Co, and O that constitute  $\text{NiCo}_2\text{O}_4$ , and a small amount of Ir and C are clearly indicated by the spectrum. Using Gaussian fitting and peak fitting, the Ni 2p emission spectrum (Fig. 4b) may be fitted to three kinds of valence states in the as-prepared composite including  $\text{Ni}^0$ ,  $\text{Ni}^{2+}$ ,  $\text{Ni}^{3+}$ , and also two shake-up satellites (peaks at 861.4 and 879.1 eV) [33,34]. The peaks at 854.4 and 871.9 eV correspond to  $\text{Ni}^{2+}$  [34,35]. The peaks around 855.9 and 873.8 eV are assigned to  $\text{Ni}^{3+}$  [36]. This means that not only  $\text{Ni}^{2+}$  but also  $\text{Ni}^{3+}$  are present in the Ni-Co oxide. From further analysis, trace amount of  $\text{Ni}^0$  also exists in our composite as indicated by the peaks at 854 and 870 eV [37]. As shown in Fig. 4c, Co is present in two oxidation states, i.e.,  $\text{Co}^{3+}$  (779.4 and 794.3 eV) and  $\text{Co}^{2+}$  (780.7 and 795.8 eV) [38], and the two shake-up type peaks at 788 and 804 eV are satellite peaks for Co [39]. Interestingly, the Ir 4f emission spectrum shown in Fig. 4d shows that elements

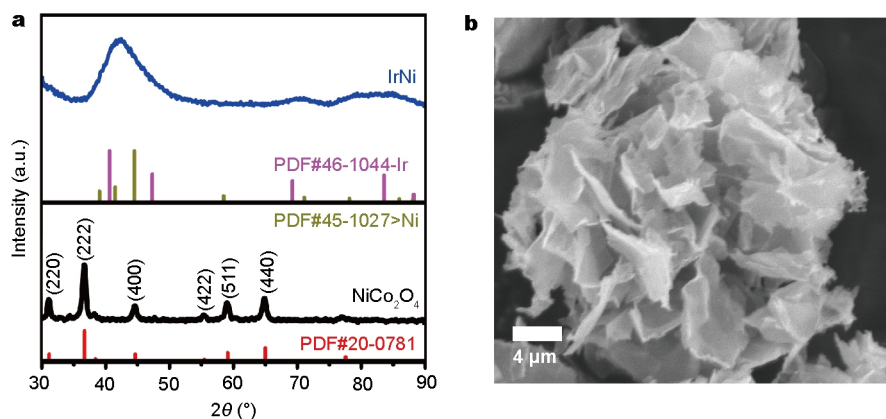


**Figure 1** (a) XRD patterns of  $\text{NiCo}_2\text{O}_4$  and IrNi alloy, (b) SEM image of  $\text{NiCo}_2\text{O}_4$ .

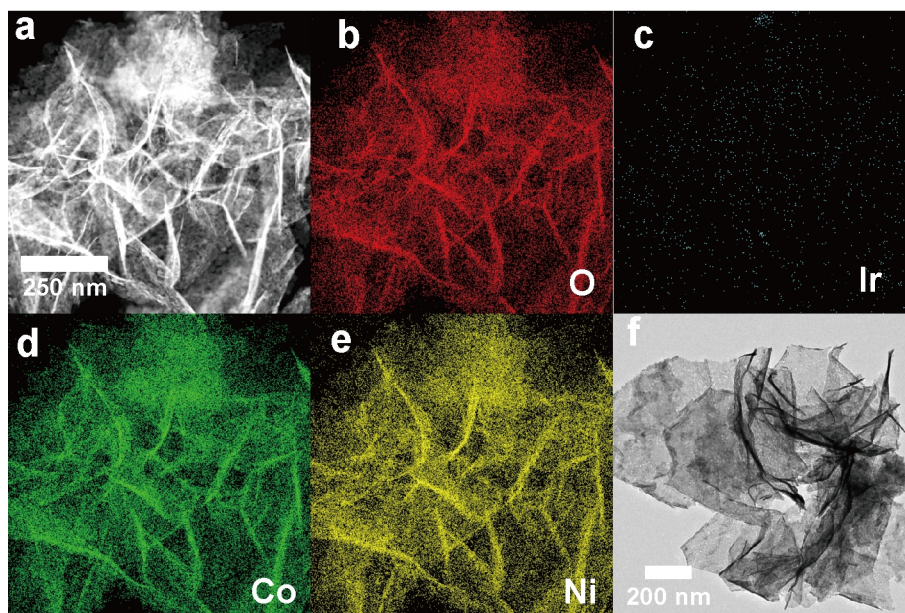


**Figure 2** (a) STEM image of IrNi/NiCo<sub>2</sub>O<sub>4</sub>; (b–e) elemental mappings of Ni, Co, O and Ir respectively; (f) TEM image of IrNi/NiCo<sub>2</sub>O<sub>4</sub>.

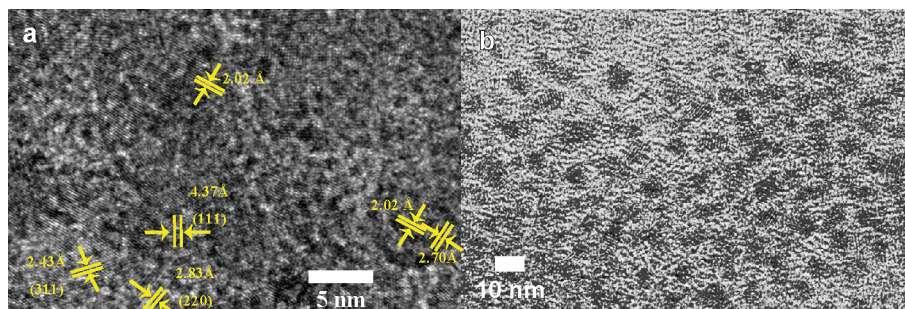


**Figure 3** (a) Lattice fringe of the composite, including several lattice spacings; (b) HRTEM image of the IrNi bimetal.

in several valence states exist in the composite we prepared, including Co<sup>2+</sup> 3p at 60.7 eV [40], Co<sup>3+</sup> 3p at 61.1 eV [41], Ir<sup>0</sup> 4f at 62.0 eV [42], Ni<sup>0</sup> 3p<sup>3/2</sup> at 65.66 eV [43], and Ni<sup>2+</sup> 3p at 67.96 eV [33]. These valences correspond in a one-to-one manner to multiple oxide NiCo<sub>2</sub>O<sub>4</sub> compounded with an IrNi alloy. The O 1s emission spectrum shown in Fig. 4e presents three types of O. The fitting peak for O1 at the binding energy of 529.2 eV is a typical of metal–oxygen bonds (M–O–M) [44], including Ni–O, Co–O and Ir–O. The fitting peak of O2 at 531.1 eV indicates defects, contaminants, and a number of surface species [45]. Finally, the peak at 532.5 eV indicates minimum physical adsorbed and chemisorbed water on the material surface (O–H) [38,46]. From the above XPS results, we can conclude that the as-prepared composite is combined with Ni<sup>0</sup>, Ni<sup>2+</sup>, Ni<sup>3+</sup>, Co<sup>2+</sup>, Co<sup>3+</sup>, and Ir, so the detailed formula can be expressed as [NiIr]/Ni<sub>1-x</sub>Ni<sub>x</sub><sup>2+</sup>Ni<sub>x</sub><sup>3+</sup>Co<sub>2-x</sub>Co<sub>x</sub><sup>3+</sup>O<sub>4</sub> (0 < x < 1). The XPS spectra

of the pure bimetallic alloy IrNi is shown in Fig. S4. Here, the binding energy for Ir 4f deviates from that of the Ir of the composite, which may be because Ir has a weak interaction with NiCo<sub>2</sub>O<sub>4</sub>, increasing the binding energy for Ir.

For electrochemical measurement, LSV was utilized to evaluate the performance of the IrNi/NiCo<sub>2</sub>O<sub>4</sub> catalysts in the OER in comparison to other catalysts (such as pure NiCo<sub>2</sub>O<sub>4</sub>, IrNi/C, and IrNi/Co<sub>3</sub>O<sub>4</sub>) because we wanted to evaluate whether the composite was superior to the materials before composition. The preparation of Co<sub>3</sub>O<sub>4</sub>, IrNi/Co<sub>3</sub>O<sub>4</sub>, and IrRh are given in the Supplementary information. The main evaluation indexes involved are the onset potential, the overpotential at 2 mA cm<sup>-2</sup> (hereafter termed  $\eta_2$ ), the current density at the overpotential of 540 mV (hereafter termed  $I_{540}$ ), Tafel slopes, and turnover frequency (TOF).

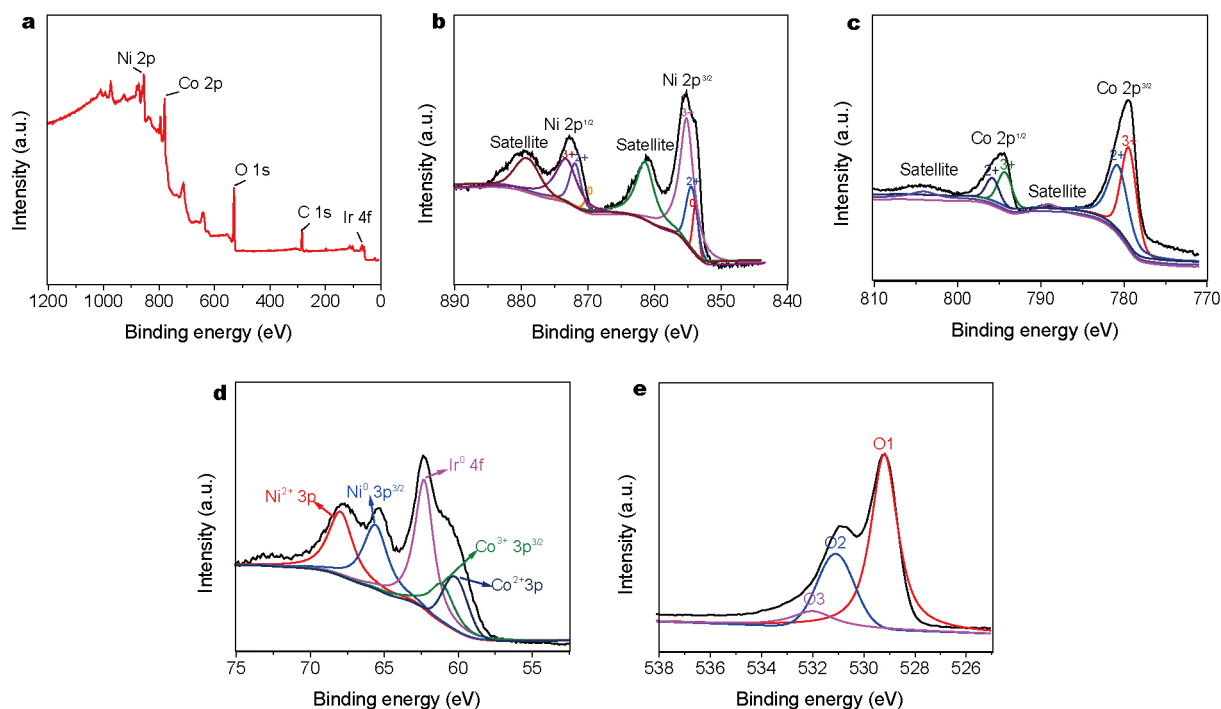


**Figure 4** (a) XPS survey spectrum of the IrNi/NiCo<sub>2</sub>O<sub>4</sub>. High-resolution XPS spectra of (b) Ni 2p; (c) Co 2p; (d) Ir 4f; and (e) O 1s.

In Fig. 5, several datagrams of electrochemical performance are shown, including comparisons between the composite and its components, different ratios of bimetal, NiCo<sub>2</sub>O<sub>4</sub>, and Co<sub>3</sub>O<sub>4</sub>, and different bimetals. The data calculated for the main indexes of these catalysts are given in Table 1. IrNi/NiCo<sub>2</sub>O<sub>4</sub> exhibits the lowest onset overpotential, lowest overpotential at 2 mA cm<sup>-2</sup>, and highest current density among these catalysts. Both pure NiCo<sub>2</sub>O<sub>4</sub> and IrNi/C present relatively weaker electrocatalytic activity, but once they are combined to form one composite, the activity is enhanced greatly. This is partly owing to the synergy effect between bimetal Ir and Ni. Ir as one kind of transition metal is rich in d-orbital electrons. When combined with Ni, the d band center of Ir will be raised and the transmission efficiency of electrons can be improved [47,48]. In addition, the Ni contained in the bimetallic IrNi provides united active sites via weak interaction with NiCo<sub>2</sub>O<sub>4</sub>. The IrNi bimetallic alloy has plentiful vacant orbitals, while the electronegativity of O atom is sufficient and O atoms contain enough outer-layer electrons. Thus, the metal of the alloy and the oxygen of NiCo<sub>2</sub>O<sub>4</sub> can interact by weak forces. Compared with the individual components, the composite contains far more stable and united active sites. Fig. 6 shows a simple proposed scheme for the structure. This synergy effect is also indicated in Fig. 5d, which shows that IrRh has

much weaker electrocatalytic activity towards the OER than that of IrNi. As shown in Fig. 5b, the OER current density for IrNi/NiCo<sub>2</sub>O<sub>4</sub> is significantly superior to that of the nanoflake IrNi/Co<sub>3</sub>O<sub>4</sub>, and the best ratio of Ir to Ni in the bimetal is 1:1, as shown in Fig. 5c. We also compared our material with other catalysts in the reported literature, demonstrating the superior activity of IrNi/NiCo<sub>2</sub>O<sub>4</sub> in several indexes, especially onset overpotential. The elimination of polarization in our material makes it highly efficient towards the OER, which means that the catalyst is activated significantly via compounding.

As is well known, the potential is directly proportional to polarization current within the area of weak polarization, while the potential is directly proportional to the logarithm of the polarization current ( $\log j$ ) within the area of strong polarization. We plotted the Tafel lines ( $\eta = b * \log j + a$ , where  $b$  is the Tafel slope) within the area of strong polarization as revealed by LSV in Fig. 7a and calculated the Tafel slopes as an approximate straight line. The Tafel slope of IrNi/NiCo<sub>2</sub>O<sub>4</sub> is approximately 98 mV decade<sup>-1</sup>, which is lower than that of the other catalysts. A lower Tafel slope indicates a more efficient electrode transport performance for oxhydroly oxidation.

TOF is calculated by the equation  $TOF = J \times A / nFm$ .  $J$  is the current density at an overpotential of 0.3 V (A cm<sup>-2</sup>),  $A$  is the area of the working electrode,  $n$  is the number of

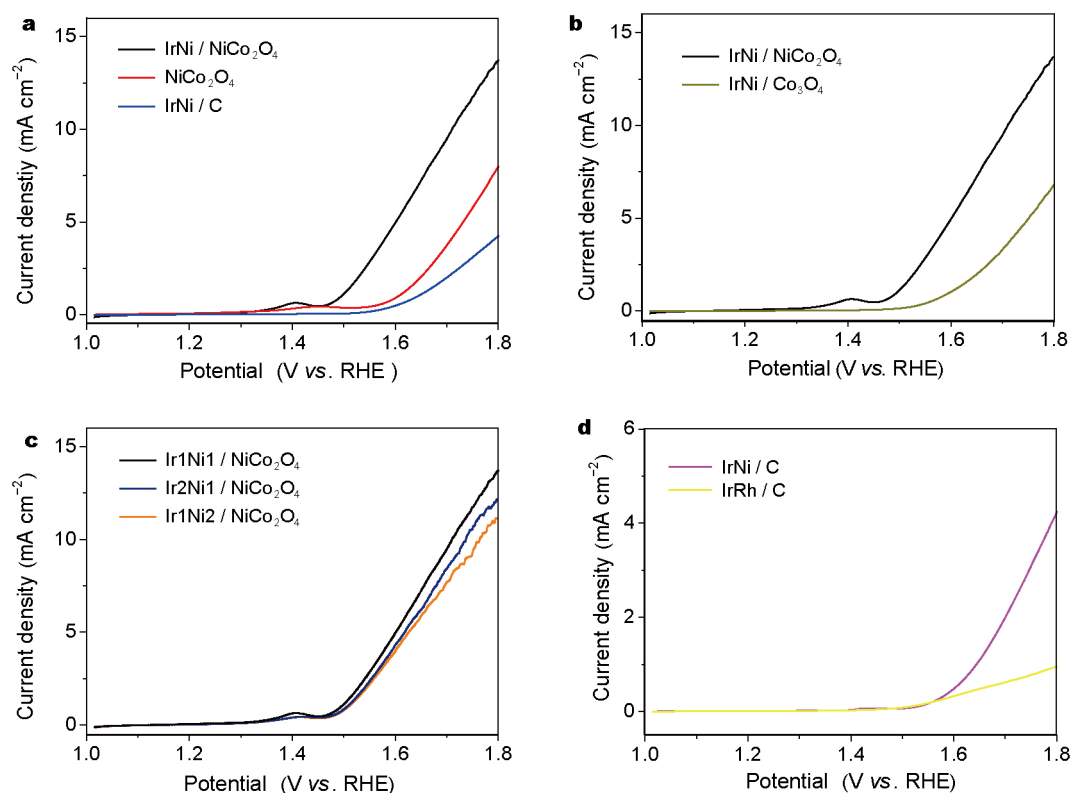


**Figure 5** Electrochemical performance towards the OER. LSV of the electrocatalysts (a) IrNi/NiCo<sub>2</sub>O<sub>4</sub>, NiCo<sub>2</sub>O<sub>4</sub>, and IrNi; (b) IrNi/NiCo<sub>2</sub>O<sub>4</sub> and IrNi/Co<sub>3</sub>O<sub>4</sub>; (c) different Ir: Ni ratios of the IrNi/NiCo<sub>2</sub>O<sub>4</sub> composites, and (d) IrNi/C and IrRh/C in KOH at pH 13 (the scanning rate is 5 mV s<sup>-1</sup>).

**Table 1** The main electrochemical indexes of several electrocatalysts

Catalyst	Onset overpotential (mV)	$\eta_2$ (mV)	$I_{540}$ (mA cm <sup>-2</sup> )
IrNi/NiCo <sub>2</sub> O <sub>4</sub>	210	290	12.78
NiCo <sub>2</sub> O <sub>4</sub>	280	420	6.65
IrNi/C	370	470	3.54
IrNi/Co <sub>3</sub> O <sub>4</sub>	300	420	5.67
Zn-Co-LDH <sup>a)</sup>	340	/	11.6
Co-OH <sup>b)</sup>	330	453	5.5
Co-monomisperse <sup>c)</sup>	270	410	~10.0
NiCo <sub>2</sub> O <sub>4</sub> /Graphene <sup>d)</sup>	310	/	~11.0

a) Sample as catalyst was reported in the Ref. [49]. b) Sample as catalyst was reported in the Ref. [12]. c) Sample as catalyst was reported in the Ref. [50]. d) Sample as catalyst was reported in the Ref. [51].

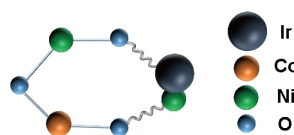


**Figure 6** Schematic diagram of NiCo<sub>2</sub>O<sub>4</sub> compounding with IrNi.

electrons transferred during the reaction (this is a four-electron reaction, so  $n = 4$ ),  $F$  is the Faraday constant (96485 C mol<sup>-1</sup>), and  $M$  is the number of moles of the active material on the glassy carbon electrode. Here we assume that

the Faraday efficiency is 100 % and each atom (including cobalt, nickel, and iridium) is the active site for the OER. TOF is a kind of index to evaluate catalytic performance. As shown in Fig. 7b, IrNi/NiCo<sub>2</sub>O<sub>4</sub> exhibits a TOF  $1.6 \times 10^{-2}$  at an overpotential of 0.38 V, which is much higher than that of the other catalysts, i.e., pure NiCo<sub>2</sub>O<sub>4</sub> ( $3.1 \times 10^{-3}$ ), Co<sub>3</sub>O<sub>4</sub> ( $3.5 \times 10^{-3}$ ), and IrNi/C ( $4.3 \times 10^{-4}$ ). The same result is also observed at high overpotentials. The Tafel slopes and TOF data both indicate that IrNi/NiCo<sub>2</sub>O<sub>4</sub> is an outstanding electrocatalyst for splitting water to obtain oxygen.

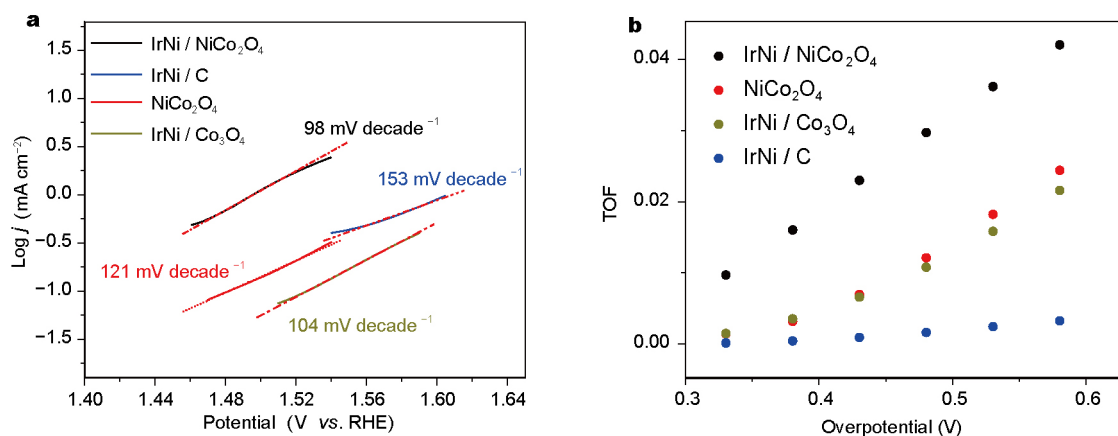


**Figure 7** (a) Tafel lines of the four electrocatalysts corresponding to the LSV curves in Figs 5a and b; (b) TOF data of the four electrocatalysts at different overpotentials.

To investigate the effect of electrolyte pH, we also evaluated these catalysts under different concentrations of KOH (from 0.1 to 0.5 mol L<sup>-1</sup>) by plotting the Tafel lines and calculating the Tafel slopes. Following several analyses,  $m_{\text{OH}^-}$  (i.e.,  $\partial \log i / \partial \log a_{\text{OH}^-}$ ) under an overpotential of 0.29 V was obtained, as shown in the insert of Fig. 8b. The current density of the OER increases with an increase in concentration of KOH. Fig. 8b shows that the Tafel slopes at all four different concentrations are much lower ( $\approx 90$  mV decade<sup>-1</sup>) at low overpotential than at high potential ( $\approx 250$  mV decade<sup>-1</sup>). This is because the adsorption of more OH<sup>-</sup> decreases the number of active sites for the OER at higher potential. The value at low potential ( $b = 90$  mV decade<sup>-1</sup>) is approximately  $2.303 \times 5RT/3F$ . These data will be used in the following study and further analysis.

Based on a report by Lyons *et al.* [21], we adopted both experimental and kinetic mechanism analysis to rationalize the results we obtained. First, the mechanism of the OER can be generalized into two parts. The elementary reactions of these two parts are formulated as Scheme 1.

Typically, steps a4 and b4 are regarded as the rate-determining step (RDS). For further research, we combined the two parts from steps C3 to C5, which correspond to steps a3, a4, and a5 (or b3, b4, and b5).

Through the interaction of the two individual components, it is possible for the catalyst to provide more active sites and more easily form a superoxide band because of the introduction of Ir. Then, we use the electrochemical kinetics parameters briefly given below. The step C3 can be expressed as:

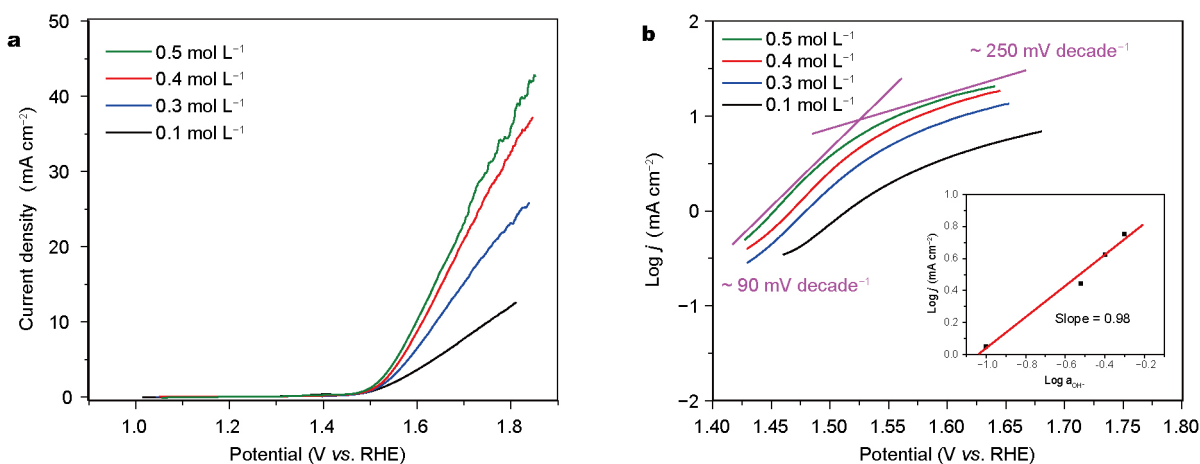
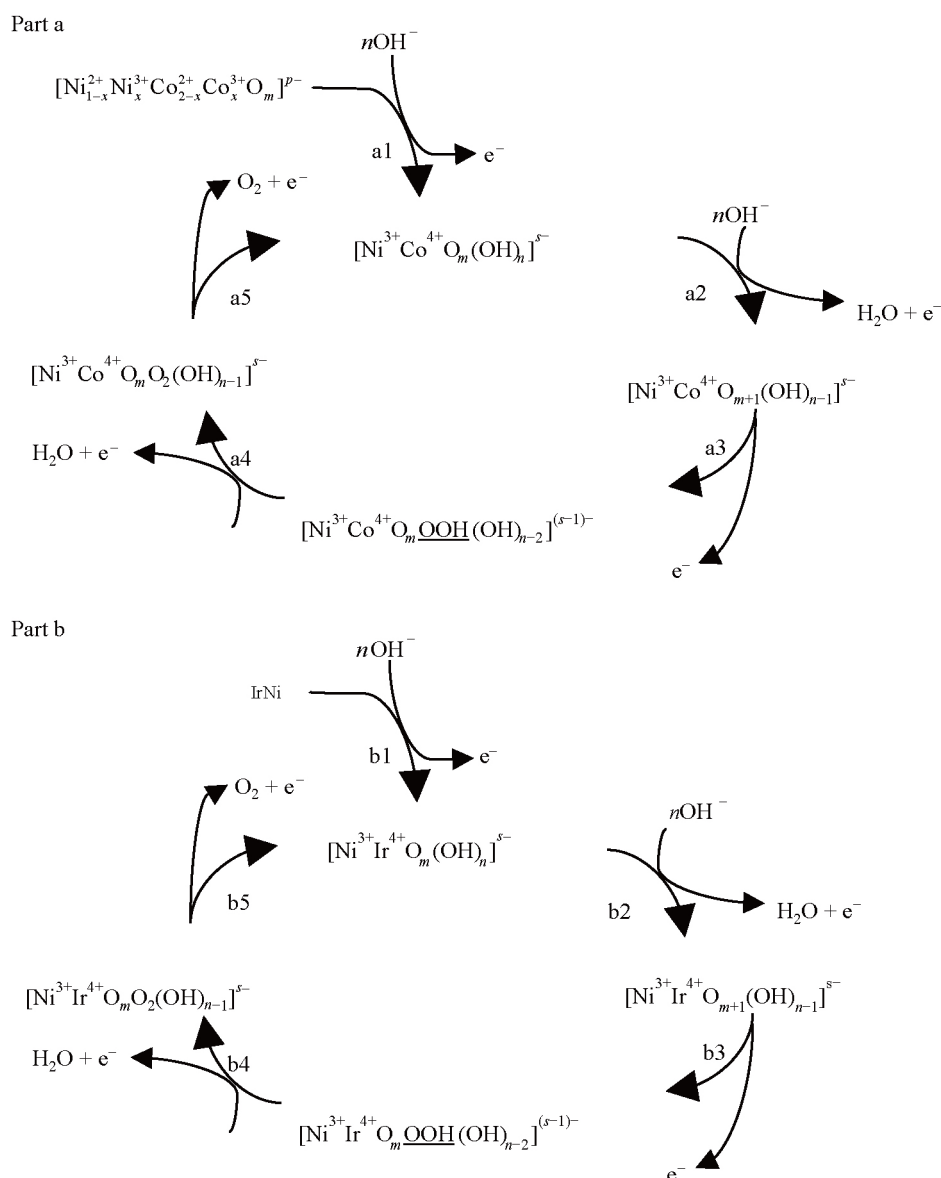


**Figure 8** (a) LSV curves of IrNi/NiCo<sub>2</sub>O<sub>4</sub> under different concentrations of KOH at a scanning rate of 5 mV s<sup>-1</sup>. (b) Tafel lines for IrNi/NiCo<sub>2</sub>O<sub>4</sub> in different concentrations of KOH corresponding to the LSV curves in Fig. 8a. The inset image is the reaction order plot from the polarization data at an overpotential of 290 mV.



**Scheme 1** The elementary reactions of the two parts for the mechanism of OER.

$$\bar{l}_a = \bar{k}_a^0 F a_{\text{OH}^-} (1 - \theta) \exp(-\beta \eta F / RT), \quad (1)$$

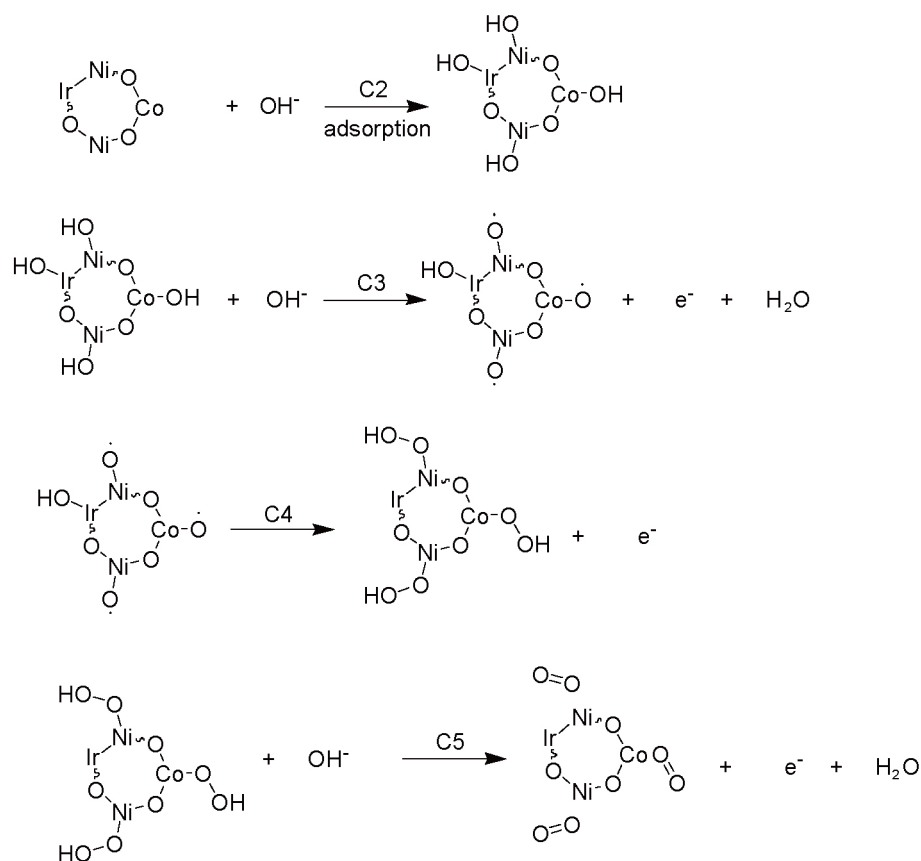
$$\bar{l}_a = \bar{k}_a^0 F \theta \exp(-(1 - \beta) \eta F / RT). \quad (2)$$

$$\begin{aligned} \theta &= \frac{\bar{k}_a^0 a_{\text{OH}^-} \exp(\eta F / RT)}{\bar{k}_a^0 + \bar{k}_a^0 a_{\text{OH}^-} \exp(\eta F / RT)} \\ &= K^0 a_{2\text{OH}^-} \exp(\eta F / RT) \ll 1, \end{aligned} \quad (3)$$

where  $\theta$  denotes the coverage of the electrode surface. Assuming that  $\bar{l}_a = \bar{l}_a$ , then we can easily obtain the parameter of step C4:

$$\begin{aligned} \bar{l}_a &= \bar{k}_a^0 F \theta \exp\left(\frac{\beta \eta F}{RT}\right) \\ &= K^0 \bar{k}_a^0 a_{\text{OH}^-} \exp[(1 + \beta) \eta F / RT]. \end{aligned} \quad (4)$$

If we assume  $\beta = 1/2$ , we obtain the Tafel slope  $b = 2.303RT / F (1 + \beta) = 0.39 \text{ mV decade}^{-1}$  and  $m_{\text{OH}^-} = 1$  theoretically. Based on the above work, we obtain the Tafel slope  $b = 2.303 \times 5RT / 3F$  and  $m_{\text{OH}^-} = 0.98$ . Compared with the theoretical result, the  $m_{\text{OH}^-}$  fits well, but the Tafel slope is significantly larger. This is probably because  $\text{OH}^-$  adsorbed on the surface raises the barrier of the reaction. However, the Tafel slope for IrNi/NiCo<sub>2</sub>O<sub>4</sub> is superior to those of the other three materials owing to the formation



of united active sites. Comparing the Tafel slopes and TOFs of IrNi/NiCo<sub>2</sub>O<sub>4</sub>, IrNi, and NiCo<sub>2</sub>O<sub>4</sub>, which are the composite and individual parts, respectively, the synergy effect between the two parts clearly plays an important role in the whole reaction. Therefore decorating NiCo<sub>2</sub>O<sub>4</sub> with bimetallic IrNi is an effective way to enhance its catalytic activity towards the OER.

## CONCLUSION

We successfully synthesized flower-shaped NiCo<sub>2</sub>O<sub>4</sub> using a microwave-assisted method, and decorated it with IrNi alloy nanoparticles to prepare an electrocatalyst for the OER. SEM and TEM indicated that the flower-shaped NiCo<sub>2</sub>O<sub>4</sub> nanostructures were assembled from ultrathin nanoflakes, and HRTEM as well as XPS revealed the composition of the prepared IrNi/NiCo<sub>2</sub>O<sub>4</sub>. A series of electrochemical measurements were used to evaluate the electrocatalytic activity of IrNi/NiCo<sub>2</sub>O<sub>4</sub> towards the OER. The electrocatalytic activities of other catalysts were included for comparison. Owing to the flower-shaped structure and introduction of IrNi alloy nanoparticles, IrNi/NiCo<sub>2</sub>O<sub>4</sub> presented a relatively lower overpotential and a higher current density (about 13 mA cm<sup>-2</sup>). The flower-shaped 3D structure provides a high surface area

for supporting IrNi alloy nanoparticles, and offers more active sites for the adsorption of -OH. Tafel slopes also verified the more efficient electron transport performance of IrNi/NiCo<sub>2</sub>O<sub>4</sub>. Furthermore, IrNi/NiCo<sub>2</sub>O<sub>4</sub> showed a higher turnover ratio for the OER to the number of atoms from the TOF profile. In summary, this is an efficient method to enhance the electrocatalytic activity towards the OER by employing 3D NiCo<sub>2</sub>O<sub>4</sub> nanostructures and decoration with a relatively cheap IrNi alloy catalyst.

Received 3 October 2016; accepted 15 November 2016;  
published online 23 December 2016

- 1 Wang J, Cui W, Liu Q, *et al.* Recent progress in cobalt-based heterogeneous catalysts for electrochemical water splitting. *Adv Mater*, 2016, 28: 215–230
- 2 Ehteshami SMM, Vignesh S, Rasheed RKA, *et al.* Numerical investigations on ethanol electrolysis for production of pure hydrogen from renewable sources. *Appl Energy*, 2016, 170: 388–393
- 3 Koper MTM. Hydrogen electrocatalysis: a basic solution. *Nat Chem*, 2013, 5: 255–256
- 4 Norskov JK, Rossmeisl J, Logadottir A, *et al.* Origin of the overpotential for oxygen reduction at a fuel-cell cathode. *J Phys Chem B*, 2004, 108: 17886–17892
- 5 Chen S, Zhao Y, Sun B, *et al.* Microwave-assisted synthesis of mesoporous Co<sub>3</sub>O<sub>4</sub> nanoflakes for applications in lithium ion batteries and oxygen evolution reactions. *ACS Appl Mater Interfaces*, 2015, 7: 3306–3313

- 6 Irshad A, Munichandraiah N. High catalytic activity of amorphous Ir-Pi for oxygen evolution reaction. *ACS Appl Mater Interfaces*, 2015, 7: 15765–15776
- 7 Jeon HS, Jee MS, Kim H, *et al.* Simple chemical solution deposition of  $\text{Co}_3\text{O}_4$  thin film electrocatalyst for oxygen evolution reaction. *ACS Appl Mater Interfaces*, 2015, 7: 24550–24555
- 8 Masud J, Swesi AT, Liyanage WPR, *et al.* Cobalt selenide nanostructures: an efficient bifunctional catalyst with high current density at low coverage. *ACS Appl Mater Interfaces*, 2016, 8: 17292–17302
- 9 Sun W, Song Y, Gong XQ, *et al.* Hollandite structure  $\text{K}_{x=0.25}\text{IrO}_2$  catalyst with highly efficient oxygen evolution reaction. *ACS Appl Mater Interfaces*, 2016, 8: 820–826
- 10 Reier T, Oezaslan M, Strasser P. Electrocatalytic oxygen evolution reaction (OER) on Ru, Ir, and Pt catalysts: a comparative study of nanoparticles and bulk materials. *ACS Catal*, 2012, 2: 1765–1772
- 11 Lee Y, Suntivich J, May KJ, *et al.* Synthesis and activities of rutile  $\text{IrO}_2$  and  $\text{RuO}_2$  nanoparticles for oxygen evolution in acid and alkaline solutions. *J Phys Chem Lett*, 2012, 3: 399–404
- 12 Li Y, Zhang L, Xiang X, *et al.* Engineering of ZnCo-layered double hydroxide nanowalls toward high-efficiency electrochemical water oxidation. *J Mater Chem A*, 2014, 2: 13250–13258
- 13 Wang D, Chen X, Evans DG, *et al.* Well-dispersed  $\text{Co}_3\text{O}_4/\text{Co}_2\text{MnO}_4$  nanocomposites as a synergistic bifunctional catalyst for oxygen reduction and oxygen evolution reactions. *Nanoscale*, 2013, 5: 5312–5315
- 14 Yeo BS, Bell AT. Enhanced activity of gold-supported cobalt oxide for the electrochemical evolution of oxygen. *J Am Chem Soc*, 2011, 133: 5587–5593
- 15 Liang Y, Li Y, Wang H, *et al.*  $\text{Co}_3\text{O}_4$  nanocrystals on graphene as a synergistic catalyst for oxygen reduction reaction. *Nat Mater*, 2011, 10: 780–786
- 16 Elumalai P, Vasanth HN, Munichandraiah N. Electrochemical studies of cobalt hydroxide—an additive for nickel electrodes. *J Power Sources*, 2001, 93: 201–208
- 17 Gong M, Dai H. A mini review of NiFe-based materials as highly active oxygen evolution reaction electrocatalysts. *Nano Res*, 2015, 8: 23–39
- 18 Wang HY, Hsu YY, Chen R, *et al.*  $\text{Ni}^{3+}$ -induced formation of active  $\text{NiOOH}$  on the spinel Ni-Co oxide surface for efficient oxygen evolution reaction. *Adv Energy Mater*, 2015, 5: 1500091
- 19 Friebel D, Louie MW, Bajdich M, *et al.* Identification of highly active Fe sites in (Ni, Fe)OOH for electrocatalytic water splitting. *J Am Chem Soc*, 2015, 137: 1305–1313
- 20 Kinoshita K. *Electrochemical Oxygen Technology*. New York: John Wiley & Sons, 1992, 30
- 21 Lyons MEG, Brandon MP. A comparative study of the oxygen evolution reaction on oxidised nickel, cobalt and iron electrodes in base. *J Electroanal Chem*, 2010, 641: 119–130
- 22 Meng Y, Wang K, Zhang Y, *et al.* Hierarchical porous graphene/polyaniline composite film with superior rate performance for flexible supercapacitors. *Adv Mater*, 2013, 25: 6985–6990
- 23 Han F, Li WC, Li MR, *et al.* Fabrication of superior-performance  $\text{SnO}_2/\text{C}$  composites for lithium-ion anodes using tubular mesoporous carbon with thin carbon walls and high pore volume. *J Mater Chem*, 2012, 22: 9645–9651
- 24 Wang X, Han X, Lim M, *et al.* Nickel cobalt oxide-single wall carbon nanotube composite material for superior cycling stability and high-performance supercapacitor application. *J Phys Chem C*, 2012, 116: 12448–12454
- 25 Xia XH, Tu JP, Zhang YQ, *et al.* Three-dimensional porous nano-Ni/Co(OH)<sub>2</sub> nanoflake composite film: a pseudocapacitive material with superior performance. *J Phys Chem C*, 2011, 115: 22662–22668
- 26 Chatterjee S, Nafezarefi F, Tai NH, *et al.* Size and synergy effects of nanofiller hybrids including graphene nanoplatelets and carbon nanotubes in mechanical properties of epoxy composites. *Carbon*, 2012, 50: 5380–5386
- 27 Zeng Y, Liu P, Du J, *et al.* Increasing the electrical conductivity of carbon nanotube/polymer composites by using weak nanotube–polymer interactions. *Carbon*, 2010, 48: 3551–3558
- 28 Chen B, Zhu Z, Guo Y, *et al.* Facile synthesis of mesoporous Ce–Fe bimetal oxide and its enhanced adsorption of arsenate from aqueous solutions. *J Colloid Interface Sci*, 2013, 398: 142–151
- 29 Lee JP, Chen D, Li X, *et al.* Well-organized raspberry-like Ag@Cu bimetal nanoparticles for highly reliable and reproducible surface-enhanced Raman scattering. *Nanoscale*, 2013, 5: 11620–11624
- 30 Mondal AK, Su D, Chen S, *et al.* A microwave synthesis of mesoporous  $\text{NiCo}_2\text{O}_4$  nanosheets as electrode materials for lithium-ion batteries and supercapacitors. *ChemPhysChem*, 2015, 16: 169–175
- 31 Zhu Y, Cao C, Zhang J, *et al.* Two-dimensional ultrathin  $\text{ZnCo}_2\text{O}_4$  nanosheets: general formation and lithium storage application. *J Mater Chem A*, 2015, 3: 9556–9564
- 32 Tong X, Chen S, Guo C, *et al.* Mesoporous  $\text{NiCo}_2\text{O}_4$  nanoplates on three-dimensional graphene foam as an efficient electrocatalyst for the oxygen reduction reaction. *ACS Appl Mater Interfaces*, 2016, 8: 28274–28282
- 33 Lian KK. Investigation of a “two-state” Tafel phenomenon for the oxygen evolution reaction on an amorphous Ni-Co alloy. *J Electrochem Soc*, 1995, 142: 3704–3712
- 34 Mansour AN. Characterization of NiO by XPS. *Surf Sci Spectra*, 1994, 3: 231
- 35 Shalvoy R. Characterization of coprecipitated nickel on silica methanation catalysts by X-ray photoelectron spectroscopy. *J Catalysis*, 1979, 56: 336–348
- 36 Kim JG, Pugmire DL, Battaglia D, *et al.* Analysis of the  $\text{NiCo}_2\text{O}_4$  spinel surface with Auger and X-ray photoelectron spectroscopy. *Appl Surface Sci*, 2000, 165: 70–84
- 37 Salvati L, Makovsky LE, Stencel JM, *et al.* Surface spectroscopic study of tungsten-alumina catalysts using X-ray photoelectron, ion scattering, and Raman spectroscopies. *J Phys Chem*, 1981, 85: 3700–3707
- 38 Marco JF, Gancedo JR, Gracia M, *et al.* Characterization of the nickel cobaltite,  $\text{NiCo}_2\text{O}_4$ , prepared by several methods: an XRD, XANES, EXAFS, and XPS study. *J Solid State Chem*, 2000, 153: 74–81
- 39 Tan BJ, Klabunde KJ, Sherwood PMA. XPS studies of solvated metal atom dispersed (SMAD) catalysts. Evidence for layered cobalt-manganese particles on alumina and silica. *J Am Chem Soc*, 1991, 113: 855–861
- 40 Allen GC, Harris SJ, Jutson JA, *et al.* A study of a number of mixed transition metal oxide spinels using X-ray photoelectron spectroscopy. *Appl Surface Sci*, 1989, 37: 111–134
- 41 McIntyre NS, Cook MG. X-ray photoelectron studies on some oxides and hydroxides of cobalt, nickel, and copper. *Anal Chem*, 1975, 47: 2208–2213
- 42 Crist BV. *XPS Handbook: Elements & Native Oxides*. New York: John Wiley & Sons, 2007
- 43 Mansour AN. Nickel monochromated Al Ka XPS spectra from the physical electronics model 5400 spectrometer. *Surf Sci Spectra*, 1994, 3: 221
- 44 Choudhury T, Saied SO, Sullivan JL, *et al.* Reduction of oxides of iron, cobalt, titanium and niobium by low-energy ion bombard-

- ment. *J Phys D-Appl Phys*, 1989, 22: 1185–1195
- 45 Roginskaya YE, Morozova OV, Lubnin EN, *et al.* Characterization of bulk and surface composition of  $\text{Co}_x\text{Ni}_{1-x}\text{O}_y$  mixed oxides for electrocatalysis. *Langmuir*, 1997, 13: 4621–4627
- 46 Menezes PW, Indra A, González-Flores D, *et al.* High-performance oxygen redox catalysis with multifunctional cobalt oxide nanochains: morphology-dependent activity. *ACS Catal*, 2015, 5: 2017–2027
- 47 Boissel V, Tahir S, Koh CA. Catalytic decomposition of  $\text{N}_2\text{O}$  over monolithic supported noble metal-transition metal oxides. *Appl Catalysis B-Environ*, 2006, 64: 234–242
- 48 Qun S, Landong L, Zhengping H, *et al.* Highly active and stable bimetallic Ir/Fe-USY catalysts for direct and NO-assisted  $\text{N}_2\text{O}$  decomposition. *Appl Catalysis B-Environ*, 2008, 84: 734–741
- 49 Zou X, Goswami A, Asefa T. Efficient noble metal-free (electro)catalysis of water and alcohol oxidations by zinc–cobalt layered double hydroxide. *J Am Chem Soc*, 2013, 135: 17242–17245
- 50 Wu L, Li Q, Wu CH, *et al.* Stable cobalt nanoparticles and their monolayer array as an efficient electrocatalyst for oxygen evolution reaction. *J Am Chem Soc*, 2015, 137: 7071–7074
- 51 Lee DU, Kim BJ, Chen Z. One-pot synthesis of a mesoporous  $\text{NiCo}_2\text{O}_4$  nanoplatelet and graphene hybrid and its oxygen reduction and evolution activities as an efficient bi-functional electrocatalyst. *J Mater Chem A*, 2013, 1: 4754

**Acknowledgments** This work was supported by the National Natural Science Foundation of China (61371021 and 61671284). The authors also acknowledge the support of Shanghai Education Commission (Peak Discipline Construction).

**Author contributions** Xu J conceived and design the experiments; Chen Z performed the experiments; Chen Z and Zhao H analyzed the data. All authors contributed to the general discussion.

**Conflict of interest** The authors declare that they have no conflict of interest.

**Supplementary information** The experimental data are available in the online version of the paper.



**Hongbin Zhao** is an associate professor at Shanghai University. He received his MSc degree in environmental science and engineering from Dalian Jiaotong University in 2006. Then he pursued his PhD degree in applied chemistry at Shanghai Jiaotong University. He worked at the Department of Material Science and Engineering, Shanghai University as a postdoctor from 2009 to 2011. He joined Shanghai University as an associate professor since 2011. From 2014 to 2015, he worked at the Department of Chemical Engineering, University of Waterloo (Canada) as a visiting scholar. His research focuses on electrochemical energy storage/transfer and nanostructured energy materials, including noble metal (Pt, Pd, Ru) catalysts in PEMFA fuel cell, micro-nanoporous carbon (graphene, conducting polymer) on lithium-sulfur batteries, rechargeable aqueous hybrid batteries and supercapacitor.



**Jiujun Zhang** is the President of the College of Science in Shanghai University and a Senior Research Officer and Catalysis Core Competency Leader at the National Research Council of Canada Institute for Fuel Cell Innovation (NRC-IFCI, now changed to Energy, Mining & Environment Portfolio (NRC-EME)). Dr. Zhang received his BSc and MSc degrees in electrochemistry from Peking University in 1982 and 1985, respectively, and his PhD degree in electrochemistry from Wuhan University in 1988.



**Jiaqiang Xu** obtained his BSc degree in chemistry from Zhengzhou University, MSc degree in inorganic chemistry from the University of Science and Technology of China (USTC) and PhD degree in material science from Shanghai University, respectively. He has been a professor in chemistry since 2001. Currently, he is the director of China Special Committee on Gas and Humidity Sensor Technologies. His research interests include the synthesis of nanomaterials and their applications in gas sensors and other fields.

## 铱镍纳米颗粒修饰的花状钴酸镍: 其可控合成以及对于氧析出反应的电化学活性增强

陈志范<sup>1</sup>, 赵宏滨<sup>1\*</sup>, 张久俊<sup>1</sup>, 徐甲强<sup>1,2\*</sup>

**摘要** 本文制备了一种双金属IrNi修饰的花状NiCo<sub>2</sub>O<sub>4</sub>复合材料,并研究了其对于氧析出反应的电化学活性,结果显示其电化学活性明显提升. NiCo<sub>2</sub>O<sub>4</sub>和IrNi分别通过水热法和热分解法制备,再通过超声复合,使得双金属附着在复合氧化物表面. 通过与纯NiCo<sub>2</sub>O<sub>4</sub>, IrNi以及IrNi/Co<sub>3</sub>O<sub>4</sub>相比较,所制备的IrNi/NiCo<sub>2</sub>O<sub>4</sub>对于氧析出反应的性能最为优异. 在各个参数指标中,拥有最低的过电势210 mV,在540 mV的过电势下具有最高的电流密度. 电子转移数和塔菲尔斜率分析表明该复合材料由于修饰上了双金属材料,极大地降低了极化,具有更高效的电子转移速率. 此外本文还对电催化机理进行了研究,发现复合材料结合反应位点有效改善了反应速率决定步骤. 其中,协同效应起着至关重要的作用,这一效应明显提高电子传输效率的同时提供了更多的活性位点. IrNi/NiCo<sub>2</sub>O<sub>4</sub>是一种出色的氧析出反应电催化剂.